Experimental Analysis of Physical Interacting Objects of a Building at mmWave Frequencies

Khosravi, Hedieh; Cai, Xuesong; Tufvesson, Fredrik

Published in:
18th European Conference on Antennas and Propagation, EuCAP 2024

2024

Document Version:
Peer reviewed version (aka post-print)

Experimental Analysis of Physical Interacting Objects of a Building at mmWave Frequencies

Hedieh Khosravi, Xuesong Cai, Fredrik Tufvesson
Department of Electrical and Information Technology, Lund University, Lund, Sweden.
Email: {hedieh.khosravi, xuesong.cai, fredrik.tufvesson}@eit.lth.se

***Abstract*—Understanding the evolution of multipath components (MPCs) in real radio channels is crucial to enhancing channel modeling and multipath-assisted positioning. This paper provides an experimental analysis of the behavior of MPCs originating from a standard building facade at millimeter wave (mmWave) frequencies. Utilizing a high-resolution channel parameter estimation method alongside a joint clustering and tracking technique, we identify physical interacting objects and analyze their lifetimes and quantities. The building wall under study is shown to have many distributed distinct backscattering points and reflection contributions due to the windows. Our findings shed light on the reflection and scattering patterns from standard building elements, highlighting the importance of including them in channel models, positioning methods, and ray tracing simulations.**

***Index Terms*—Millimeter wave, Multipath component (MPC), cluster, lifetime, visibility region, clustering and tracking, birth-and-death process**

I. Introduction

Millimeter-wave (mmWave) channels are increasingly being explored in wireless communications, localization, and sensing. This is mainly due to the available bandwidth, higher inherent temporal resolution, and increased directivity when paired with massive multiple-input multiple-output (MIMO) antenna systems [1], [2]. A critical component in this development is understanding the behavior of its multipath components (MPCs). Studying the evolution of MPCs is not only vital for channel characterization and modeling, but also crucial for accurate multipath-assisted mmWave positioning [3], [4]. Our research contributes to this field by analyzing the behavior of mmWave MPCs in a realistic measurement scenario with standard walls, highlighting the evolution of MPCs and the interaction with physical structures. The 28 GHz 256×128 MIMO mmWave channel sounder utilized in our study provides highly refined double-directional angular and delay resolution [5]. When paired with a high-resolution channel parameter estimation algorithm based on space-alternating generalized expectation maximization (SAGE) [6], [7], we achieve state-of-the-art accuracy in capturing the evolution of MPCs. Subsequently, MPCs with channel parameters that are close to each other are grouped into clusters. These identified clusters are then tracked over time, providing information on the number of trackable clusters and their lifetime. Lastly, we localize the corresponding physical interacting objects in order to better understand the mmWave propagation in a common environment.

The remainder of the paper is organized as follows. Section I presents an overview of the measurement campaign. Section II is dedicated to channel data processing and is divided into three sub-sections. The channel model and parameter estimation, clustering and tracking algorithm, and physical interacting object identification method are presented in these subsections, respectively. All results are presented and discussed in Section III. Finally, the paper concludes in Section IV. Throughout the paper, column vectors are represented by boldface lowercase letters and $(\cdot)^{\mathsf{T}}$ denotes the matrix transpose.

II. Measurement Campaign

A measurement campaign was conducted in a courtyard, as depicted in Fig. 1. This courtyard is surrounded by brick walls, including multiple rows of reflective windows. The courtyard spans the dimension of 35.75×15 m^2. The equipment used for the measurements is a mmWave switched array sounder [5]. This channel sounder was operated with a center frequency of 28 GHz and a bandwidth of 768 MHz.

On the transmitter (Tx) side, we used a 16×4 dual-polarized planar array, covering a 180-degree field of view. On the receiver (Rx) side, we used a cylindrical antenna array, constituted by eight panels, each with 4×4 dual-polarized patch antennas, allowing for a complete 360-degree field of view (Tx/Rx arrays are shown in Fig. 1).

The Tx array is placed facing the front wall of the courtyard in a fixed location, as shown in Fig. 1. Meanwhile, the Rx moves along an L-shaped trajectory, approximately 28 meters in length, which is marked in Fig. 1. Along this receiver trajectory, nine windows of the right wall are passed, and three windows of the front wall are passed. The widths of these windows are approximately 1.5 meters, and they are spaced about 1.5 meters apart from each other. The windows, made of metalized insulated glazing, are expected to serve as reflective objects for radio propagation. Fig. 2 shows an overview of the courtyard, with the expected major interacting objects of the environment marked and the RX trajectory. The channel impulse response was recorded every 10 cm, resulting in a total of 280 measured snapshots.

This work was partially supported by the Vinnova/FFI project Beyond 5G positioning, Connected Systems, the Wallenberg AI, Autonomous Systems and Software Program (WASP) funded by the Knut and Alice Wallenberg Foundation, the Horizon Europe Framework Programme under the Marie Skłodowska-Curie (Grant No.101059091), and the Swedish Research Council (Grant No. 2022-04691). We thank Juan Sanchez and Javad Ebrahimi for their assistance during the measurements.

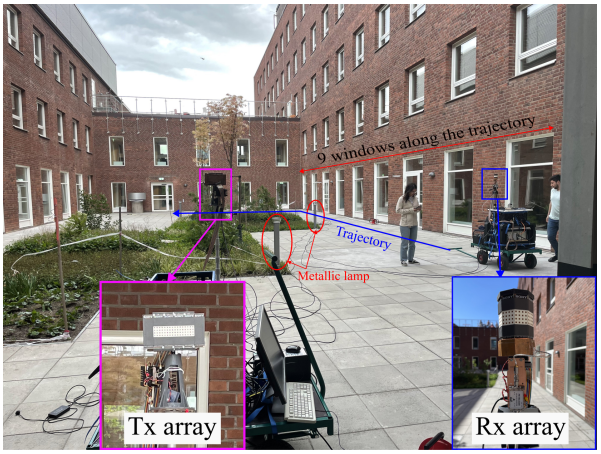

Fig. 1: A picture of the measurement environment including the Tx and Rx setups, taken when the Rx is at the starting point.

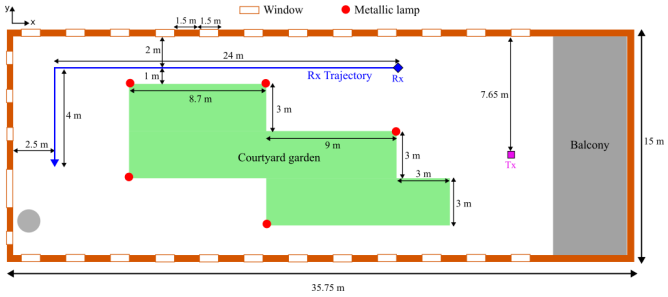

Fig. 2: Schematic overview of the measurement area.

Furthermore, a lidar sensor (visible in Fig. 1) was used to record the position and orientation of the receiver.

III. Channel Data Processing

A. Channel Parameter Estimation

We consider a channel model being a superposition of L specular MPCs characterized by their parameters as $\boldsymbol{\theta}_l = [\boldsymbol{\alpha}_l, \tau_l, \phi_{T,l}, \theta_{T,l}, \phi_{R,l}, \theta_{R,l}]^T, l \in \{1, ..., L\}$, which are the complex polarimetric path amplitudes, path delay, azimuth and elevation Angle of Departure (AoD), and the azimuth and elevation Angle of Arrival (AoA) of the lth MPC, respectively. The measured channel transfer function at snapshot time index n, carrier frequency index f, transmit antenna index n_T, and receive antenna index n_R, can be represented as

$$H_{n_T,n_R}(n,f) = \sum_{l=1}^{L} \boldsymbol{b}^T_{R,n_R}(\phi_{R,l},\theta_{R,l},f) \begin{bmatrix} \alpha_{HH,l} & \alpha_{HV,l} \\ \alpha_{VH,l} & \alpha_{VV,l} \end{bmatrix} \boldsymbol{b}_{T,n_T}(\phi_{T,l},\theta_{T,l},f) \times b(f) e^{-j2\pi f \tau_l} + N(n,f), \tag{1}$$

where $\boldsymbol{b_{R,n_R}} \in \mathbb{C}^{2\times 1}$ and $\boldsymbol{b_{T,n_T}} \in \mathbb{C}^{2\times 1}$ are the complex polarimetric antenna responses of the n_R-th receiver antenna and the n_T-th transmitter antenna at each arrival/departure angle, respectively, which are obtained using the effective aperture distribution function (EADF) of the sounder antenna arrays [8]. $\alpha_{HH,l}, \alpha_{HV,l}, \alpha_{VH,l}$, and $\alpha_{VV,l}$, the elements of $\boldsymbol{\alpha}_l$, are the complex gains of the lth MPC with respect to horizontal to horizontal, horizontal to vertical, vertical to horizontal, and vertical to vertical polarization, respectively. Furthermore, $b(f)$ represents the response of the measurement system without antenna arrays, which can be obtained from the back-to-back measurements, and N denotes white Gaussian noise. A computationally efficient SAGE-based channel estimation algorithm was applied to estimate the parameters, $\boldsymbol{\theta_l}$, of L specular MPCs. Up to $L = 60$ MPCs were extracted; the power levels of the MPCs are above the noise threshold. All estimated parameters were then calibrated and transformed into a common coordinate system, which was chosen to be the lidar coordinate system. A gradual delay drift was identified during the post-processing of the data and was compensated for using the estimated delay of the line-of-sight component and the lidar data. The AOAs and AODs are transformed from the Rx/Tx local coordinate system into the lidar coordinate system. The calibrated MPC parameters shown in Fig. 4 can be used to locate the corresponding physical interacting objects in the environment.

B. Clustering and Tracking

The MPC distance (MCD) is a metric for quantifying multipath separation, initially introduced in [9]. Then this metric was used [10], [11] to identify clusters within a snapshot and also track them over time by associating those MPCs with sufficiently close MCDs between neighboring snapshots. The MCD between two MPCs i and j, $i, j \in \{1, ..., L\}$, is defined as

$$\text{MCD}_{i,j} = \sqrt{\text{MCD}^2_{\text{AoD},i,j} + \text{MCD}^2_{\text{AoA},i,j} + \text{MCD}^2_{\tau,i,j}}, \tag{2}$$

where $\text{MCD}_{\text{AoD},i,j}$, $\text{MCD}_{\text{AoA},i,j}$, and $\text{MCD}_{\tau,i,j}$ are the MPC distance between MPC i and j in angular and delay domains, standardized and transformed in such a way that they can be mutually compared. They are defined as

$$\text{MCD}_{\text{AoD/AoA},i,j} = \frac{1}{2} \left\| \begin{bmatrix} \cos\phi_{T/R,i} \sin\theta_{T/R,i} \\ \sin\phi_{T/R,i} \sin\theta_{T/R,i} \\ \cos\theta_{T/R,i} \end{bmatrix} - \begin{bmatrix} \cos\phi_{T/R,j} \sin\theta_{T/R,j} \\ \sin\phi_{T/R,j} \sin\theta_{T/R,j} \\ \cos\theta_{T/R,j} \end{bmatrix} \right\| \tag{3}$$

and

$$\text{MCD}_{\tau,i,j} = \zeta . |\tau_i - \tau_j|, \tag{4}$$

where ζ is a scaling factor to balance the weights of the delay and angular domains. The optimal setting should be determined considering the physical relationship between changes in propagation distance due to delay and angular variations. Hence, it could be a tunable scaling factor with respect to the propagation distance. An MCD threshold-based clustering and tracking algorithm based on [12] was applied to the SAGE estimation results. The clustering step for each snapshot is performed by grouping MPCs that have not yet been grouped, with their MCDs smaller than a predefined threshold ($\sigma_{\text{clustering}}$) in an iterative manner. Subsequently,

the tracking step is performed by evaluating the cluster centroids between neighboring positions. A cluster centroid is determined as the power-weighted mean of the MPC parameters within that cluster. The overall procedure involves the following steps:

1) Cluster initialization: wherein MPCs are iteratively assigned to clusters if their distance to the current reference point is less than $\sigma_{\text{clustering}}$. The current reference point is determined as the MPC with the highest power among the remaining MPCs.
2) The minimization of overall intra-cluster MCDs is achieved by utilizing the previous cluster centroids as new reference points and iteratively updating the cluster centroids.
3) Cluster tracking: If a cluster in the previous snapshot and a cluster in the current snapshot are mutually close, with their MCD below a predefined tracking threshold σ_{tracking}, they are associated as a tracked cluster.
4) A previous cluster that remains un-associated is considered a "dead" cluster, while a current cluster lacking associations is regarded as a "born" cluster.

Hence, as a result, we would have K_n identified clusters at each snapshot time index n, represented by their centroids as $\boldsymbol{\mu}_k = [\alpha_k, \tau_k, \phi_{T,k}, \theta_{T,k}, \phi_{R,k}, \theta_{R,k}]^T, k \in \{1, ..., K_n\}$. The grouped MPCs, i.e. the clusters, are expected to correspond to one physical interacting object. The visibility of the corresponding physical interacting object can also be obtained using the tracking results.

C. Physical Interacting Objects Identification

Fig. 3 shows the 3D geometry of the physical interacting point with a first-order reflection assumption, where $\boldsymbol{p} = [x, y, z]^T$ is the position of a physical interacting point at one snapshot. The known positions of Tx and Rx in that snapshot are shown as $\boldsymbol{p}_{Tx} = [x_t, y_t, z_t]^T$ and $\boldsymbol{p}_{Rx} = [x_r, y_r, z_r]^T$, respectively. The position of the physical interacting point, $\boldsymbol{p}$, can be estimated by incorporating all available information, i.e., the estimated delay(τ), AOA(ϕ_R, θ_R), and AoD (ϕ_T, θ_T) that could correspond to the parameters estimated by SAGE, $\boldsymbol{\theta}_l, l \in \{1, ..., L\}$, or the clustered parameters $\boldsymbol{\mu}_k, k \in \{1, ..., K\}$. Ultimately, the following set of geometrical equations is valid.

$$
\begin{aligned}
&\|\boldsymbol{p} - \boldsymbol{p}_{Tx}\| + \|\boldsymbol{p} - \boldsymbol{p}_{Rx}\| = c_0\tau, \\
&\arctan(\frac{y - y_t}{x - x_t}) = \phi_T, \\
&\frac{\pi}{2} - \arctan(\frac{z - z_t}{\sqrt{(x - x_t)^2 + (y - y_t)^2}}) = \theta_T, \\
&\arctan(\frac{y - y_r}{x - x_r}) = \phi_R, \\
&\frac{\pi}{2} - \arctan(\frac{z - z_r}{\sqrt{(x - x_r)^2 + (y - y_r)^2}}) = \theta_R,
\end{aligned}
\tag{5}
$$

where $\|.\|$ is the Euclidean norm and c_0 is the speed of light. This set of information leads to an overdetermined system, and the position of the physical interacting point $\boldsymbol{p}$ can be estimated using an iterative weighted nonlinear least-squares method. We classify the set of L estimated MPCs into two distinct groups: those that meet the criteria to satisfy the first-order reflection assumption and those that do not. The criterion we employ is based on the minimum distance between two vectors, $\vec{\boldsymbol{u}}_t$ and $\vec{\boldsymbol{u}}_r$, pointing to the AoD and AoA directions, respectively. If this distance exceeds a specified threshold, we categorize the MPC as a higher-order reflection MPC.

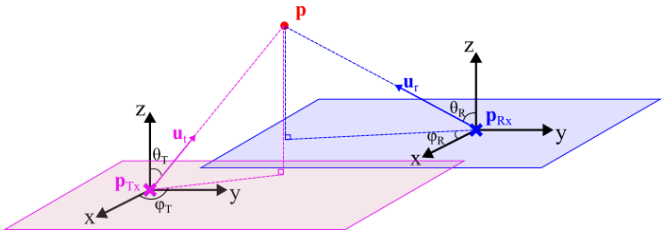

Fig. 3: Physical interacting point geometry, with the first-order-reflection assumption.

IV. Results

Fig. 4 shows the estimated MPCs along the measurement trajectory. This figure illustrates the overall evolution of the MPCs across the delay, azimuth AOD, and azimuth AOA domains. As expected, the propagation distance of the LoS path initially increased and then remained relatively constant after passing the turning point of the trajectory. Given that the Tx and Rx were approximately at the same elevation, the estimated elevation AOD and AOA of the MPCs are mainly in a 20-degree sector centered at 90 degrees. Fig. 5 shows the centroids of the clusters in delay and azimuth AOD and azimuth AOA. The number of tracked MPCs and their lifetimes can be seen in each domain.

Fig. 6 shows the location of the identified physical interacting points using the estimated MPCs for the first 5 meters of the trajectory. For geometric reference, three planes representing the ground of the courtyard, the right wall, and the front wall are highlighted. As can be seen, all nine windows on the right wall are identified with their individual physical interacting points, collectively numbered as group 1, albeit with a decaying power-level contribution. By zooming into the region of the wall adjacent to the Rx odometry, it becomes evident that there are two distinct sets of high-power physical interacting points, separated by a height difference of approximately 1 meter, along the width of the nearby window, i.e., 1.5 meters. After passing the window, there is a decrease in the power level as the physical interacting points transition from the window to the adjacent brick wall. The 1.5-meter gap between this set of strong reflection points and the preceding set to the right aligns with the separation distance between the windows. The previous set is shorter because its corresponding window was only partially visible during movement. This pattern is repeated throughout the entire trajectory as the Rx passes each window. In Fig. 6, only the first five meters of the trajectory are illustrated, which does not allow for the observation of the repeated pattern across the entire trajectory. However, by examining

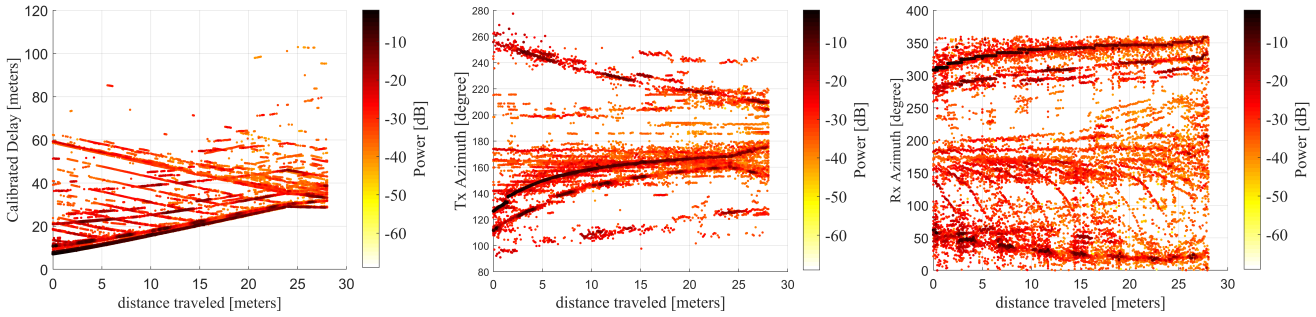

Fig. 4: Calibrated SAGE-estimated parameters of all MPCs over all snapshots, where x-axis is the distance traveled by Rx. (a) Propagation distance. (b) Tx azimuth. (c) Rx azimuth.

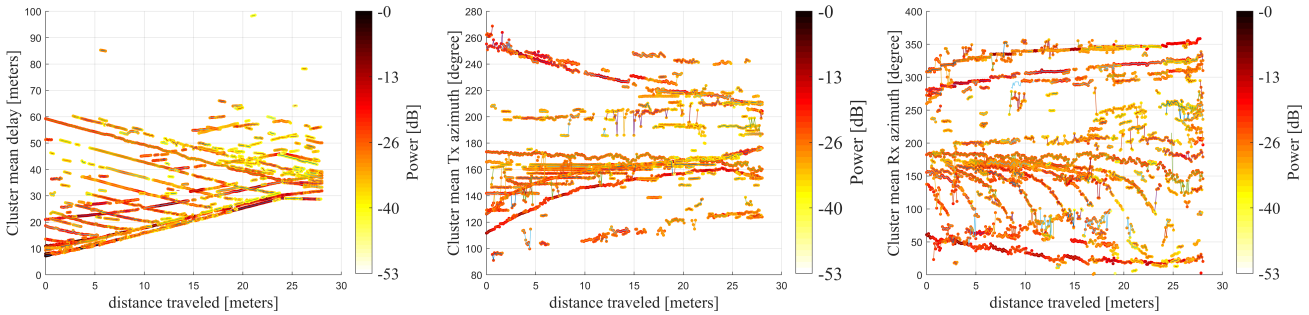

Fig. 5: Clustering and tracking results in (a) propagation distance, (b) Tx azimuth, and (c) Rx azimuth domains.

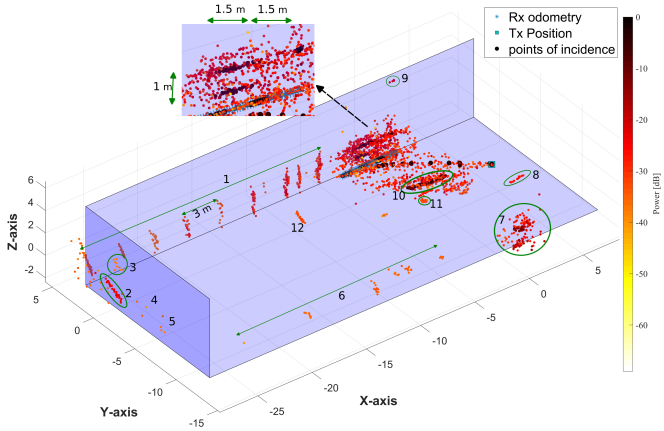

Fig. 6: 3D visualization of the localized physical interacting objects using the estimated MPC parameters of the first 5 meters of the Rx trajectory.

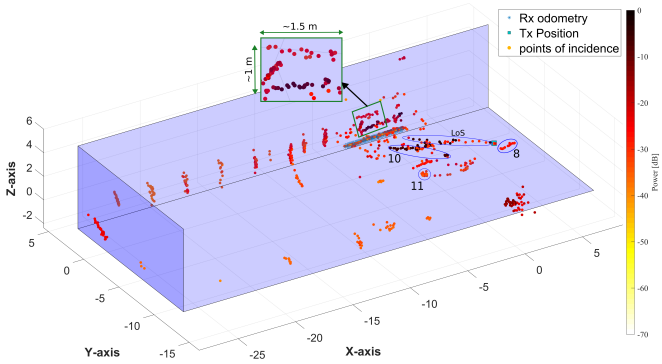

Fig. 7: 3D visualization of the localized physical interacting objects using the clustered parameters of the first 5 meters of the Rx trajectory.

the extracted MPCs over the whole trajectory in Fig. 4 in one domain, e.g., delay, we find 9 high-power (black color) fragments, each around 1.5 meters long, lying on a long relatively lower power (red color) line very close to the LOS path. This confirms that each of those black fragments represents the strong reflection contribution from each of the 9 windows on the right wall as the Rx passes by them, while the underlying relatively lower power (red color) components correspond to the contribution from the bricks of the right wall. Furthermore, this observation confirms that the parallel lines with a negative slope in the delay domain, see Fig. 4a, result from the backscattering of each window ahead of the Rx. Since each of these lines with a negative slope terminating around one of the black fragments, indicating that as the Rx approaches each window, the backscattering contribution from that window comes to an end, while the strong reflection contribution from the same window begins. The backscattering contribution of the windows ahead of Rx

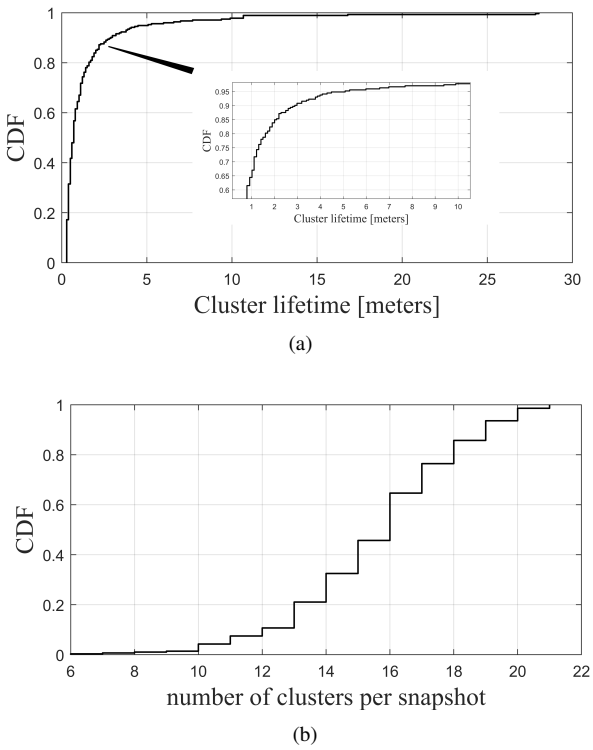

Fig. 8: Empirical cumulative distribution function for: (a) the lifetime of identified clusters; (b) the number of clusters identified per snapshot.

odometry is grouped as set number 1 in Fig.6.

A similar pattern is observed from the windows on the left wall, but with somewhat reduced power and fewer distinct windows, due to the longer propagation distance. See sets number 7 and 6 in Fig. 6. Another important physical interacting object that gives rise to high-power MPCs is the ground, as numbered in Fig. 6 as physical interacting object 10. The physical interacting points corresponding to the LOS path are located either on the TX/Rx location or along a line between those two points. This is because of the delay calibration accuracy that sometimes has ended up with a LOS propagation distance slightly shorter than the Rx and Tx position distances. The physical interacting points of the front wall labeled as 2, are always persistent (the long-tracked cluster at the top of Fig. 5a); Since one of the reflective windows on that wall is exactly located in front of the Rx trajectory. Sets number 4 and 5 represent identified physical interacting points from other windows, which have a short lifetime and visibility. The other identified physical interacting objects worth mentioning are coming from windows on the building's second floor in front, numbered 3. Sets number 8 and 9 are also the identified physical interacting objects from the second-floor windows with short lifetimes. Sets number 11 and 12 correspond to the physical interacting points of the metallic lamps marked in Fig. 1. Fig. 7 shows the identified physical interacting objects using the clustered parameters. It is evident that the interacting objects identified using the SAGE-estimated MPCs are also discernible here. To prevent misconceptions due to the 3D-to-2D projection in Fig. 7, only select close-by clusters are marked to clarify their distinct identities. The empirical cumulative distribution function (CDF) of the cluster lifetime and the number of clusters per snapshot are shown in Fig. 8a and Fig. 8b, respectively. While many of the clusters exhibit short lifetimes, a considerable number of active clusters are observed in each snapshot. This suggests that as one cluster dissipates, a new one is emerging along the trajectory.

V. Conclusion

This paper analyzed and demonstrated the evolution of MPCs that originate from a standard building facade at mmWave frequencies while moving in a trajectory along the building. MPCs are estimated using SAGE and subsequently clustered and tracked. Physical interacting objects are identified using the estimated MPCs. The results showed significant backscattering and reflection contributions from windows on the side walls. When the RX is approaching a window, there is a significant backscattering component, and when passing it, there is a relatively strong reflected component from that window. This pattern was seen from the physical interacting points of both side walls. We also presented empirical statistics on the lifetime and number of clustered physical interacting points.

References

[1] T. S. Rappaport, Y. Xing *et al.*, "Overview of millimeter wave communications for fifth-generation (5G) wireless networks—with a focus on propagation models," *IEEE Transactions on antennas and propagation*, vol. 65, no. 12, pp. 6213–6230, 2017.

[2] X. Wang, L. Kong *et al.*, "Millimeter wave communication: A comprehensive survey," *IEEE Communications Surveys & Tutorials*, vol. 20, no. 3, pp. 1616–1653, 2018.

[3] C. Gustafson, K. Haneda *et al.*, "On mm-wave multipath clustering and channel modeling," *IEEE Transactions on Antennas and Propagation*, vol. 62, no. 3, pp. 1445–1455, 2014.

[4] K. Witrisal, P. Meissner *et al.*, "High-accuracy localization for assisted living: 5G systems will turn multipath channels from foe to friend," *IEEE Signal Processing Magazine*, vol. 33, no. 2, pp. 59–70, 2016.

[5] X. Cai, E. Bengtsson *et al.*, "A switched array sounder for dynamic millimeter-wave channel characterization: Design, implementation and measurements," *submitted to IEEE Transactions on Antennas and Propagation*, 2023.

[6] X. Cai *et al.*, "Enabling complexity-efficient high-resolution parameter estimation for wideband switched array channel sounding," *Under preparation*, 2023.

[7] B. H. Fleury, M. Tschudin *et al.*, "Channel parameter estimation in mobile radio environments using the SAGE algorithm," *IEEE Journal on selected areas in communications*, vol. 17, no. 3, pp. 434–450, 1999.

[8] X. Cai, M. Zhu *et al.*, "Enhanced effective aperture distribution function for characterizing large-scale antenna arrays," *IEEE Transactions on Antennas and Propagation*, Jun. 2023.

[9] M. Steinbauer, H. Ozcelik *et al.*, "How to quantify multipath separation," *IEICE transactions on electronics*, vol. 85, no. 3, pp. 552–557, 2002.

[10] S. Cheng, M.-T. Martinez-Ingles *et al.*, "Performance of a novel automatic identification algorithm for the clustering of radio channel parameters," *IEEE Access*, vol. 3, pp. 2252–2259, 2015.

[11] N. Czink, R. Tian *et al.*, "Tracking time-variant cluster parameters in MIMO channel measurements," in *Second International Conference on Communications and Networking in China*, 2007, pp. 1147–1151.

[12] X. Cai, G. Zhang *et al.*, "Dynamic channel modeling for indoor millimeter-wave propagation channels based on measurements," *IEEE Transactions on Communications*, vol. 68, no. 9, pp. 5878–5891, 2020.